JOURNAL OF APPLIED PHYSICS VOLUME 94, NUMBER 6 15 SEPTEMBER 2003

Simulation of plasma molding over a ring on a flat surface

Doosik Kim and Demetre J. Economou[a)]
Plasma Processing Laboratory, Department of Chemical Engineering, University of Houston, Houston, Texas 77204-4004

(Received 12 February 2003; accepted 26 June 2003)

A fluid/Monte Carlo simulation model was developed to study plasma molding over an axisymmetric feature (a ring) resting on an otherwise planar surface in contact with a high-density rf plasma. The two-dimensional (r,z) time-dependent sheath potential, and ion density and flux profiles were predicted with a self-consistent fluid simulation. The trajectories of ions and energetic neutrals (resulting mainly by ion neutralization on the cylindrical sidewalls of the ring) were then followed with a Monte Carlo simulation, in an effort to obtain their energy and angular distributions on the substrate surface. When the sheath thickness was comparable to the size of the ring, strong radial electric fields deflected oncoming ions toward the sidewalls of the ring. The ion density was lower in the cylindrical well formed by the ring, compared to outside, resulting in a locally thicker sheath and a smaller spread in the double-peaked ion energy distributions at the bottom of the well. The ion impact angle increased progressively as the sidewalls were approached. The angular distribution of energetic (fast) neutrals at the bottom of the well was bimodal. The energy distribution of fast neutrals at the bottom of the well was broader compared to the parent ion energy distributions. © *2003 American Institute of Physics.* [DOI: 10.1063/1.1602573]

I. INTRODUCTION

A sheath forms over any wall in contact with plasma. The sheath over a homogeneous, flat, infinite surface is planar (one dimensional). However, when the surface contains geometrical features, the sheath tends to wrap around the contour of the features. This behavior is called *plasma molding*.[1] Appropriate length scales governing plasma molding are the sheath thickness, L_{sh}, and the size of the surface topography, D. When $L_{sh} \gg D$, the sheath edge is essentially planar as if the surface were flat (one-dimensional sheath). This situation is encountered in microelectronics fabrication, where the feature size is <1 μm while the sheath is hundredths of a μm thick. At the other extreme ($L_{sh} \ll D$), the sheath edge conforms to the surface topography, and the sheath is *locally* one dimensional. The extensive literature on one-dimensional sheaths[2–6] may be applied to both extreme cases. In the intermediate case ($L_{sh} \sim D$), the sheath edge bends gently over the contour of the feature, becoming planar far away from the feature. The ion flux, ion energy distribution (IED), and ion angular distribution (IAD) along the surface contour can be drastically different, depending on the shape of the sheath edge. Since surface reactions are normally driven by ion bombardment, the flux, energy, and angular distributions of ions over the substrate surface are critically important. Plasma molding with $L_{sh} \sim D$ may be encountered in microelectromechanical systems (MEMS) processing,[7] ion extraction through grids (ion beam sources,[8] neutral beam sources,[9] and plasma thrusters)[10] and plasma immersion ion implantation.[11] Plasma molding over steps and trenches and the resulting distributions of ions and fast neutrals has been studied, both by simulation and experiment, in several recent works.[1,12–14]

In this article, a fluid/Monte Carlo (MC) simulation of plasma molding over a Si ring (axisymmetric feature) on an otherwise flat Si surface (Fig. 1) in contact with a high-density rf argon plasma is reported. This geometry maybe of interest in MEMS fabrication or in plasma immersion ion implantation. The simulation predicts the flux, energy, and angular distributions of ions, and fast neutrals along the surface contour. The model and simulation procedures are described in Sec. II. Simulation results are discussed in Sec. III. Summary and conclusions are presented in Sec. IV. The simulation model has been validated against experimental data for plasma molding over steps[1,12] and trenches.[13]

II. MODEL AND SIMULATION PROCEDURES

A combined fluid/MC simulation was employed in order to predict the self-consistent two-dimensional (r,z) rf sheath structure, and the flux, energy, and angular distributions of ions and energetic (fast) neutrals over the surface contour. The model and simulation procedures have been reported in more detail elsewhere.[1] Therefore, only a brief discussion is presented here.

A. Fluid simulation

An electropositive high-density plasma with one type of positive ion and electrons was considered. The governing equations are the mass and momentum continuity equations for the ions, coupled with Poisson's equation for the electric potential. The Boltzmann relation was used for electrons, neglecting electron inertia. It was assumed that the ion distribution function is a drifting Maxwellian (i.e., a Maxwellian distribution in the frame of reference moving with the ion fluid velocity), and the electron distribution function is a Maxwellian. Isothermal equations of state were used for both

[a)]Electronic mail: economou@uh.edu

 © 2003 American Institute of Physics

Downloaded 09 Sep 2003 to 129.7.158.16. Redistribution subject to AIP license or copyright, see http://ojps.aip.org/japo/japcr.jsp

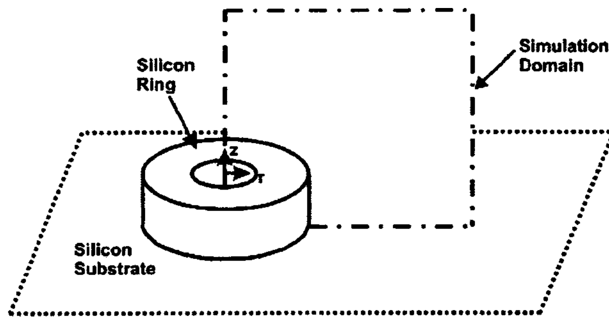

FIG. 1. Schematic of the axisymmetric surface feature considered in this study. A Si ring (500 μm high and 500 μm wide) was located on top of an otherwise planar Si substrate. The cylindrical well, enclosed by the ring, was 500 μm in diameter. The center of the well mouth was taken as the origin of the cylindrical (*r,z*) coordinate system. The simulation domain is also shown.

electrons and ions. The background neutral gas pressure and temperature (hence, density) were taken to be uniform throughout the computational domain.

The ion mass and momentum continuity equations for the axisymmetric (*r,z*) system are

$$\frac{\partial n_i}{\partial t}+\frac{1}{r}\frac{\partial}{\partial r}(rn_iu)+\frac{\partial}{\partial z}(n_i\nu)=0, \tag{1}$$

$$\frac{\partial}{\partial t}(n_iu)+\frac{1}{r}\frac{\partial}{\partial r}(rn_iuu)+\frac{\partial}{\partial z}(n_iu\nu) =-\frac{en_i}{m_i}\frac{\partial\Phi}{\partial r}-\nu_m n_i u, \tag{2}$$

$$\frac{\partial}{\partial t}(n_i\nu)+\frac{1}{r}\frac{\partial}{\partial r}(rn_i\nu u)+\frac{\partial}{\partial z}(n_i\nu\nu) =-\frac{en_i}{m_i}\frac{\partial\Phi}{\partial z}-\nu_m n_i \nu, \tag{3}$$

where n_i, m_i, u, and ν are the ion density, ion mass, radial and axial components of ion fluid velocity, respectively. Φ is the electric potential, e is the elementary charge, and ν_m is the total collision frequency for momentum exchange of ions (elastic scattering and charge exchange collisions) with the background gas. The ion pressure force was ignored because the ion temperature is much lower than the electron temperature (cold ion approximation). However, ion thermal effects were accounted for in the MC simulations.

Equation (1) can be rewritten in terms of $\xi_i=rn_i$ instead of n_i,

$$\frac{\partial \xi_i}{\partial t}+\frac{\partial}{\partial r}(\xi_iu)+\frac{\partial}{\partial z}(\xi_i\nu)=0. \tag{4}$$

Corresponding expressions derived from Eqs. (2) and (3) are

$$\frac{\partial}{\partial t}(\xi_iu)+\frac{\partial}{\partial r}(\xi_iuu)+\frac{\partial}{\partial z}(\xi_iu\nu)=-\frac{e\xi_i}{m_i}\frac{\partial\Phi}{\partial r}-\nu_m\xi_iu, \tag{5}$$

$$\frac{\partial}{\partial t}(\xi_i\nu)+\frac{\partial}{\partial r}(\xi_i\nu u)+\frac{\partial}{\partial z}(\xi_i\nu\nu)=-\frac{e\xi_i}{m_i}\frac{\partial\Phi}{\partial z}-\nu_m\xi_i\nu. \tag{6}$$

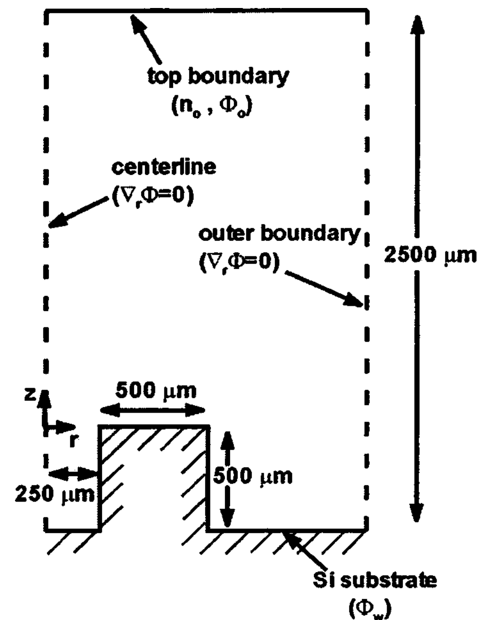

FIG. 2. Simulation domain and boundary conditions. The domain was bounded radially by the centerline and an outer boundary. The plasma density n_o and the electric potential Φ_o were specified at the top boundary. The conducting Si wall is an equipotential surface at ground potential ($\Phi_w=0$).

Equations (4)–(6) are in a divergence-free form and are easier to implement computationally.

Poisson's equation with the Boltzmann relation for electrons reads

$$\nabla^2\Phi=-\frac{e}{\varepsilon_o}\left(n_i-n_o\exp\left(\frac{\Phi-\Phi_o}{T_e}\right)\right), \tag{7}$$

where ε_o is the permittivity of free space, T_e is the electron temperature (in V), and Φ_o and n_o are the electric potential and ion density, respectively, at the top boundary (see Fig. 2).

The numerical domain and boundary conditions used in this study are shown in Fig. 2. The simulation domain is bound in the radial direction by the centerline and the outer boundary. An otherwise planar silicon (Si) substrate with a ring (500 μm high and 500 μm wide) is located at the bottom of the domain. The inner radius of the ring is 250 μm. Thus, the Si ring forms a boundary that separates a cylindrical well (500 μm in inner diameter and 500 μm in depth) from an open area. The electric potential was specified at the top boundary (Φ_o) and on the Si substrate (Φ_w). The substrate was assumed a perfect conductor (equipotential surface). The electric potential was assumed symmetric at the centerline, while the electric field points only vertically on the right-hand side boundary away from the feature (one-dimensional sheath). At the top boundary, the ion density (n_o) and electron temperature were also specified; the ion flux was linearly extrapolated based on the values at the two immediate interior nodes.[1] The location of the top boundary was far enough from the sheath edge so that the quasineutrality condition ($n_0=n_e$) was applied at that boundary. The rf plasma sheath evolved self-consistently in accordance with the specified plasma parameters (n_o, T_e, and $\Phi_o-\Phi_w$).

Downloaded 09 Sep 2003 to 129.7.158.16. Redistribution subject to AIP license or copyright, see http://ojps.aip.org/japo/japcr.jsp

The divergence-free Eqs. (4)–(6) were discretized in space using a finite difference flux-corrected transport (FCT) scheme. A weighted average of low- and high-order fluxes was used for the convective terms in Eqs. (4)–(6). The high-order flux was weighted to the maximum extent that allowed no numerical instability to be introduced. In this manner, the FCT solutions were stable and also more accurate compared to low-order solutions. The multidimensional FCT scheme developed by Zalesak was used in this study.[15] Rusanov's method, an improvement of Rax's method, was used for calculating the low-order fluxes. The Rusanov scheme introduces artificial viscosity at each nodal point and weights the importance of the neighboring mesh points, making it suitable for multidimensional simulations.[16] Second-order central difference was used for high-order fluxes. Equations (4)–(6) were integrated in time using the Adams–Bashforth second-order method. The time step was chosen so that the Courant–Friderichs–Levy condition was satisfied. After each time step, the electric potential was updated by solving Poisson's Eq. (7) by a Newton–Raphson method combined with a conjugate gradient scheme. The simulation evolved until a (periodic) steady state was reached.

B. Monte Carlo simulation

The fluid model just described can predict the self-consistent profiles of ion density and flux. The *average* energy and angle of ions impinging on the substrate can also be obtained. However, since ions can suffer collisions with the background gas, the fluid model cannot predict the energy and angular *distributions*. MC simulation was used for this purpose. The MC simulation was also used to follow fast neutrals produced by charge exchange collisions or ion neutralization on the sidewall, in an effort to predict the fast neutral energy and angular distributions as well.

In the MC simulation, ion trajectories were tracked by integrating the equations of motion

$$\frac{\partial \nu_r}{\partial t} = \frac{e}{m_i} E_r(r,z,t),$$
$$\frac{\partial \nu_z}{\partial t} = \frac{e}{m_i} E_z(r,z,t), \qquad (8)$$
$$\frac{\partial \nu_\theta}{\partial t} = 0,$$

where E_r and E_z are the radial and axial electric field, respectively, determined by the fluid simulation; ν_r, ν_z, and ν_θ are the components of the ion particle (not fluid) velocity. The corresponding equations were used for neutrals except that the right-hand side was always identically zero, since neutrals are not affected by the electric field. The spatially nonuniform electric field can be time-varying if the sheath potential oscillates. Ions were launched with the appropriate energy and angular distributions.[1] The launching position was a horizontal plane in the presheath region, away from the (curved) sheath edge. Since the ion flux was uniform along the launching plane, the number of ions launched scaled linearly with radial position. Ions were evenly distributed in the rf phase (0 to 2π) for the case of time-varying sheath potential.

TABLE I. Base parameter values used for simulations

Electron temperature, T_e	3 eV
Ion temperature, T_i[a]	0.1 eV
Transverse ion temperature, T_{tr}[a]	0.1 eV
Gas temperature	0.05 eV
Gas pressure	10 mTorr
Si wall potential, Φ_w	0 V (grounded)

[a]Used for MC simulations only. Ions were assumed cold ($T_i = T_{tr} = 0$) in the fluid simulation.

During their transit through the sheath, ions can suffer elastic scattering or charge-exchange collisions with background gas. Elastic scattering was treated as a hard sphere collision. For charge-exchange collisions, the fast ion and slow neutral switched identities to become fast neutral and slow ion, respectively, keeping their precollision velocity vector (resonant process). Both the fast neutral and slow ions were followed after the collision. However, energetic (fast) neutrals were created mainly by ion neutralization on the sidewall. Upon collision, ions were assumed to neutralize with 100% probability and to reflect specularly as fast neutrals. A binary collision model with two half scatterings[1,17] was employed to calculate the ion energy loss upon surface impact.

III. RESULTS AND DISCUSSION

The parameters varied in the simulation were the ion density n_o and the potential Φ_o at the top boundary. Other parameters were set at the base values shown in Table I. Two simulation cases are presented in this article. In the first case, the ion density was 1×10^{17} m^{-3} and the space potential was 25 V. A rf potential ($80+45\sin\omega_{rf}t$ V, $\omega_{rf}/2\pi = 13.56$ MHz) and an ion density of 5×10^{17} m^{-3} were used for the second simulation case. These simulation parameters and the resulting sheath thickness are summarized in Table II.

Figure 3 shows the ion density profile near the substrate surface for case (*i*) of Table I ($n_o = 1\times10^{17}$ m^{-3} and $\Phi_o = 25$ V). The ion density near the wall is lower by an order of magnitude compared to the value at the top boundary. The density profile varies only in the axial (vertical) direction far away from the ring, reminiscent of a one-dimensional sheath.

TABLE II. Summary of selected simulation cases. The ion density and potential were specified at the top boundary (Fig. 2). The sheath edge was defined as the position where the relative net charge density, $(n_i - n_e)/n_i$, was equal to 0.01, with the densities determined by the fluid simulation.

Simulation case	Ion density n_o (10^{17} m^{-3})	Potential Φ_o (V)	Sheath thickness[a] (μm)
(*i*)	1.0	25	312
(*ii*)	5.0	$80+45\sin\omega_{rf}t$	223

[a]The sheath thickness was calculated 1500 μm away from the center, where the sheath was one dimensional. The sheath thickness of case (*ii*) was the time-average value.

Downloaded 09 Sep 2003 to 129.7.158.16. Redistribution subject to AIP license or copyright, see http://ojps.aip.org/japo/japcr.jsp

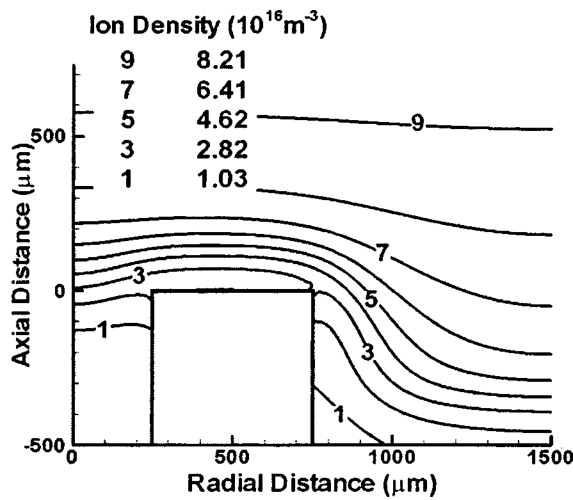

FIG. 3. Ion density profile near the Si wall for $n_o = 10^{17}$ m^{-3} and $\Phi_o = 25$ V [case (*i*) of Table II].

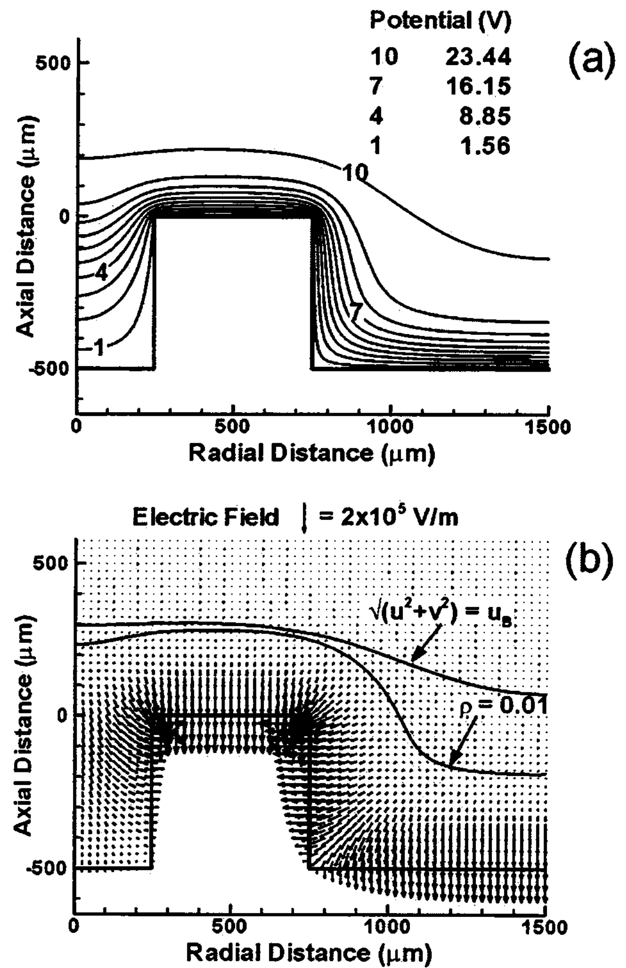

FIG. 4. Electric potential contour (a) and electric-field vector (b) plots over the ring for the condition of Fig. 3. The sheath edge is also shown in (b) using two different definitions. The upper sheath edge was defined as the locus of points at which the ion fluid speed was equal to the Bohm speed. The lower sheath edge was defined as the locus of points where the relative net charge, $(n_i - n_e)/n_i$ was equal to 0.01, with the densities determined by the fluid simulation.

Close to the ring, however, the density profile becomes two dimensional. While the plasma is in contact with an infinite flat surface away from the ring, there exists extra surface area available for ion recombination on the ring. Thus, the ion density is depleted faster near the ring. Ion depletion is even more pronounced inside the cylindrical well ($0 < r < 250$ μm), where the surface to volume ratio is even larger.

Electric potential and electric field vector profiles are shown in Figs. 4(a) and 4(b), respectively, for $n_o = 1 \times 10^{17}$ m^{-3} and $\Phi_o = 25$ V [case (*i*) of Table II]. The plasma sheath wraps around the surface topography. The sheath is almost one dimensional (planar) in the open area to the right of the ring, but it is distorted as the ring is approached. The potential is more conformal to the surface topography over the outer sidewall compared to the inner sidewall. This is due to enhanced ion depletion inside the cylindrical well ($0 < r < 250$ μm), resulting in smaller ion density (Fig. 3), thus larger Debye length and thicker sheath. In addition to the electric-field vector, the sheath edge is also plotted in Fig. 4(b). Two definitions of the sheath edge were used: (a) The location where the ion fluid *speed*, $\sqrt{(u^2 + v^2)}$, is equal to the Bohm speed, and (b) the location where the relative net charge density, $\rho \equiv (n_i - n_e)/n_i = 0.01$. According to the Bohm criterion for one-dimensional sheaths, the ion fluid speed reaches the Bohm speed, and charge neutrality still holds at the sheath edge, i.e., $n_i = n_e$ or $\rho = 0$. Thus, the sheath edge definition based on $\rho = 0.01$ yields a thinner sheath. Regardless of the definition used for the sheath edge, the electric field is very weak outside the sheath and picks up in strength as one enters the sheath [Fig. 4(b)]. The field becomes progressively stronger as the wall is approached. The electric field is mainly vertical away from the ring and in the middle section on top of the ring, but diverges along and near the sidewalls. The field is strongest on the upper corners of the ring and weakest at the inner and outer foot of the ring. The electric field is weaker along the inner sidewall compared to the outer sidewall since the ion density is lower inside the cylindrical well.

The diverging electric field and varying sheath thickness over the surface topography of Fig. 4, imply that ions will experience quite different trajectories depending on their radial position. For case (*ii*) of Table II ($n_o = 5 \times 10^{17}$ m^{-3} and $\Phi_o = 80 + 45 \sin \omega_{rf} t$ V, $\omega_{rf}/2\pi = 13.56$ MHz), a collection of ion streamlines is shown in Fig. 5. Streamlines are separated by 50 μm from each other at an axial distance $z = 700$ μm. Streamlines are mainly vertical away from the ring and on top of the ring (nearly one-dimensional sheath). However, ions entering the sheath near the sidewalls of the ring are deflected toward the sidewalls. The diverging ion flow results in an uneven distribution of ion flux over the surface topography. Figure 6 shows the time-average ion flux along the contour length. The contour length was measured along the surface, starting from the center of the bottom of the well (point A) as denoted in Fig. 6 (top) by arrow **s**. Figure 6 (bottom) shows only the normal component of the flux, namely, $n_i v$ for horizontal surfaces (AB, CD, and EF) and $n_i u$ for vertical surfaces (BC and DE). Thus, the flux profile is discontinuous at corners (points B, C, D, and E). If the ion flow were mainly vertical, the flux would be nearly uniform

Downloaded 09 Sep 2003 to 129.7.158.16. Redistribution subject to AIP license or copyright, see http://ojps.aip.org/japo/japcr.jsp

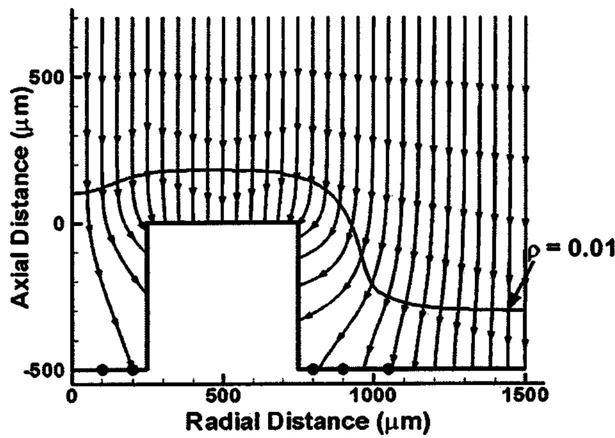

FIG. 5. Ion streamlines for case (*ii*) of Table II ($n_o = 5\times10^{17}$ m^{-3} and $\Phi_o = 80+45\sin\omega_{\rm rf}t$ V) at $t=0$. The sheath edge, defined by $\rho=0.01$, is also shown. The five dots on the horizontal surface (at radial locations 100, 200, 800, 900, and 1050 μm) represent points where MC kinetic data were collected to calculate energy and angular distributions of ions.

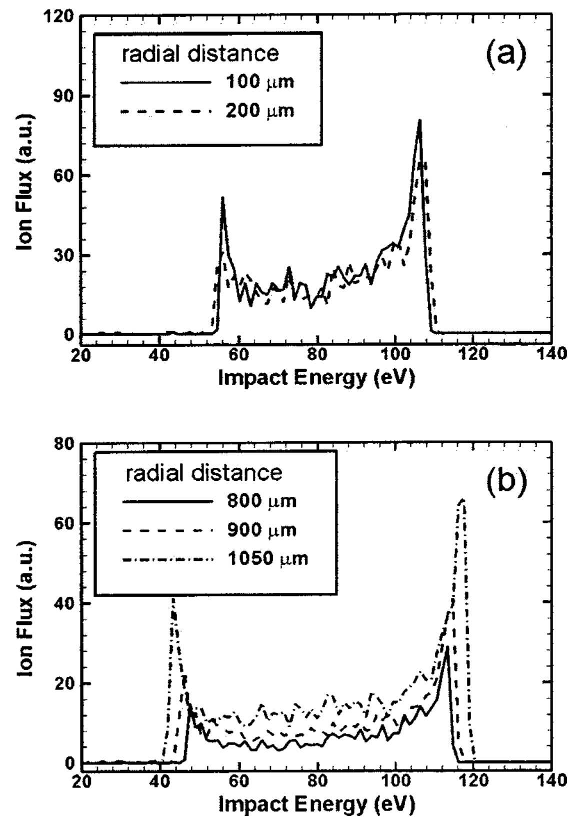

FIG. 7. IEDs, calculated by the MC simulation, at the five locations on the horizontal surface shown by dots in Fig. 5. Conditions were the same as in Fig. 5. (a) IEDs at radial positions of 100 μm and 200 μm (b) IEDs at radial positions of 800 μm, 900 μm, and 1050 μm.

on horizontal surfaces, and almost zero on the sidewalls. This case may be applicable to microelectronics processing, where the sheath thickness (hundredths of a μm) is much larger than the feature size (<1 μm) and the plasma–sheath interface is essentially planar. However, when plasma molding is significant, as shown in Fig. 6, the ion flux on the sidewalls becomes considerable, due to the diverging ion flow. As one approaches the ring from the open area (from F to E), the flux decreases monotonically from the undisturbed value (far away to the right-hand side). This situation resembles the flux distribution near a step.[1] The flux at the foot (point E) of the outer sidewall is only ~25% of the undisturbed value. The flux peaks near the upper corner (to the left of point D). There is another peak on sidewall DE. The maximum flux on the sidewall is not at the exact location of the corner (point D), although the electric-field strength is indeed maximum at that point. This is due to ion inertia. Ions are relatively massive and the ion streamlines do not necessarily follow the local electric field (nonlocal behavior). Furthermore, most of the ions entering the sheath over the cylindrical well ($0<r<250$ μm) are deflected toward the inner sidewall BC. The flux distribution along BC is similar to that along DE, except that the former flux is lower, due to lower ion densities in the well (see Fig. 3). The ion flux at the bottom of the well is very low (~6% of the undisturbed value), but it is quite uniform. The flux distribution in the well region resembles that found inside a rectangular trench.[13]

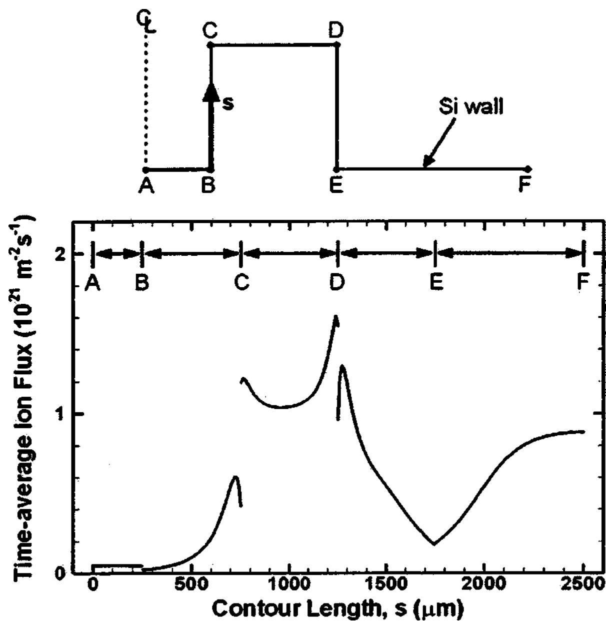

FIG. 6. Time-average ion flux (calculated by the fluid simulation) as a function of contour length, *s*, along the Si surface, under the conditions of Fig. 5. The contour length was measured starting from point A (center of the well bottom) along the surface, as shown by the thick arrow of the top figure. The flux normal to the surface is depicted; $n_i v$ for horizontal surfaces (AB, CD, and EF) and $n_i u$ for sidewalls (BC and DE), where n_i is the ion density, and u and v are the horizontal and vertical components of the ion fluid velocity, respectively. The flux is discontinuous at corner points (points B, C, D, and E).

The corresponding ion energy and angular distributions are shown in Figs. 7 and 8, respectively. These distributions were calculated by MC simulation, using the spatiotemporal electric-field profile found by the fluid simulation. Distributions were recorded at five locations (radial distance of 100, 200, 800, 900, and 1050 μm), as shown by the dots along the r axis in Fig. 5. The IEDs are double peaked, but the energy spread depends on location. The energy spread is determined by rf time ($1/\omega_{\rm rf}$) of the sheath potential and the transit time of ions through the sheath ($\tau_{\rm ion}$).[2–6] When $\omega_{\rm rf}\tau_{\rm ion}\gg 1.0$, ions

Downloaded 09 Sep 2003 to 129.7.158.16. Redistribution subject to AIP license or copyright, see http://ojps.aip.org/japo/japcr.jsp

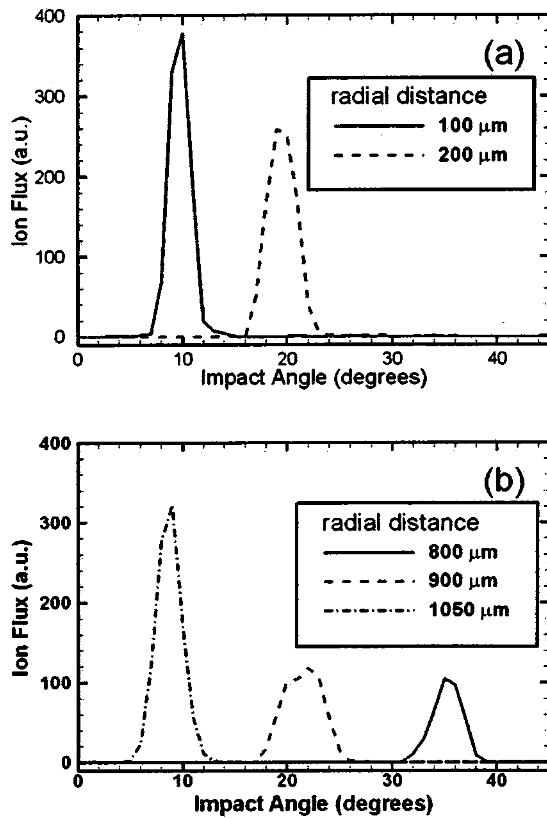

FIG. 8. IADs, calculated by the MC simulation, at the five locations on the horizontal surface shown by dots in Fig. 5. Conditions were the same as in Fig. 5. (a) IADs at radial positions of 100 μm and 200 μm (b) IADs at radial positions of 800 μm, 900 μm, and 1050 μm. The impact angle (with respect to the surface normal) was defined as $\tan^{-1}(\sqrt{(\nu_r^2+\nu_\theta^2)/\nu_z^2})$, where ν_r, ν_z, and ν_θ are the components of the ion particle (not fluid) velocity.

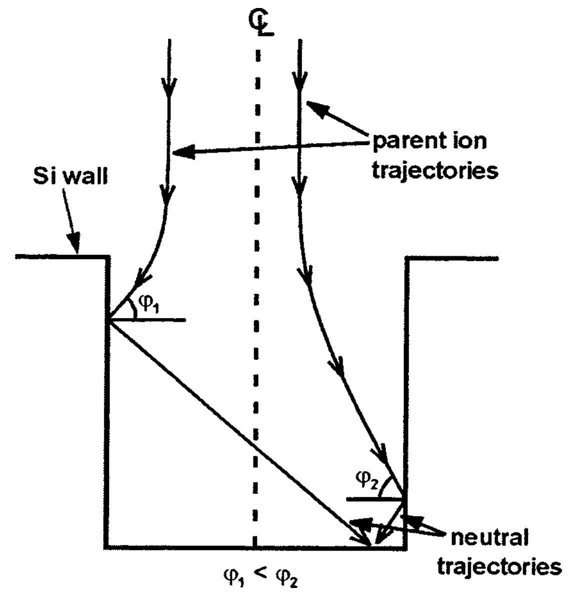

FIG. 9. Schematic of ion neutralization on the sidewall of the central well. Ions neutralize upon impact and reflect secularly as fast neutrals (incidence angle φ_i=reflection angle φ_r). Also, ions lose a fraction of their kinetic energy upon impact. The energy lost, which depends on $\pi/2-\varphi_i$, was determined by a binary collision model. Reflected neutrals strike the bottom with an angle $\pi/2-\varphi_r$ off normal.

spend enough time in the sheath to sample the time-average rf potential, resulting in single-peaked energy distributions. On the other hand, when the $\omega_{\mathrm{rf}}\tau_{\mathrm{ion}}\ll 1.0$, ions sample the instantaneous sheath potential resulting in double-peaked IEDs (assuming no collisions in the sheath) with an energy spread equal to the peak-to-peak value of the sheath potential. For intermediate values of $\omega_{\mathrm{rf}}\tau_{\mathrm{ion}}$, the energy spread decreases as $\omega_{\mathrm{rf}}\tau_{\mathrm{ion}}$ increases. For a given ω_{rf}, thicker sheaths result in a larger τ_{ion} and a smaller energy spread. This is reflected in the plots shown in Fig. 7. As the outer sidewall of the ring is approached from the open area [Fig. 7(b)], the energy spread decreases because the local sheath thickness increases (see also Fig. 5). The IEDs at the bottom of the cylindrical well are even narrower [Fig. 7(a)], since the local sheath over the well is even thicker. The IADs are also quite different on either side of the cylindrical wall of the ring. As one approaches the outer sidewall [Fig. 8(b)], the angle (with respect to the z axis) of impinging ions increases due to the diverging electric field. The average ion impact angle is $\sim$35° at radial position 800 μm (50 μm away from the outer sidewall). The IAD also shifts to larger angles as the inner sidewall is approached from the center [Fig. 8(a)]. The smaller impact angles [compared to Fig. 8(b)] are indicative of the relatively weaker deflection of the ion flow inside the well. For example, the ion impact angle is $\sim$20° at radial position 200 μm (50 μm away from the inner sidewall).

The distribution of ion flux along the substrate surface is of great importance for the application of low-temperature plasmas. For example, the etch rate is often proportional to the ion flux for ion-induced etching. The ion flux (Fig. 6), energy (Fig. 7), and angular (Fig. 8) distributions can be used to deduce the etch rate distribution along the substrate. For instance, a considerable flux on the sidewalls may cause unwanted erosion, while a smaller flux at the bottom of the cylindrical well may result in slower etching, compared to open areas.

In addition to ions, energetic (fast) neutrals must also be considered since they can also promote surface reactions. In this work, the majority of fast neutrals were produced by ion neutralization on the sidewalls. Because the background gas pressure is relatively low (10 mTorr), charge-exchange collisions in the gas phase yield only a very small fraction (a few %) of the total fast neutral population. As shown in Fig. 6, the ion flux on the sidewalls is significant. Unless they are trapped in the surface, ions will be reflected as fast neutrals and impinge on nearby surfaces. The ion neutralization process on the (inside) sidewall of the cylindrical well is shown schematically in Fig. 9. The flux, energy, and angular distributions of fast neutrals depend on the trajectory of the parent ions. It should be noted that any fast neutrals produced by ions striking the horizontal surfaces (AB and EF of Fig. 6) were not considered, since these ions are likely to be trapped and lose most of their kinetic energy to the surface. Also, reflection of fast neutrals was not considered.

Figure 10 shows the (time-average) angular and energy distributions of fast neutrals on the bottom of the well, at radial position 200 μm, for case (*ii*) of Table II (n_o=5

Downloaded 09 Sep 2003 to 129.7.158.16. Redistribution subject to AIP license or copyright, see http://ojps.aip.org/japo/japcr.jsp

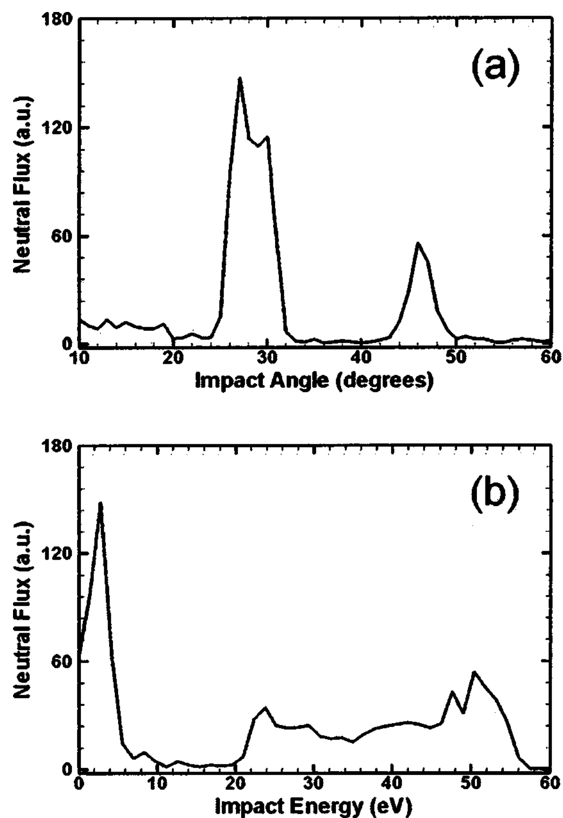

FIG. 10. Angular (a) and energy (b) distributions, calculated by the Monte Carlo simulation, of fast neutrals on the bottom of the well, 200 μm away from the centerline. Simulation conditions were the same as for Fig. 5 ($n_o = 5\times10^{17}$ m^{-3} and $\Phi_o = 80+45 \sin \omega_{rf}t$ V; case (*ii*) of Table II). The impact angle is with respect to the surface normal.

$\times10^{17}$ m^{-3} and $\Phi_o = 80+45 \sin \omega_{rf}t$ V). The angular distribution has two distinguishable features, one centered at ~46° and the other centered around 28° off the surface normal [Fig. 10(a)]. The feature at larger angles seems to originate from ions impinging on the upper part of the (inner) sidewall (left-hand side trajectory in Fig. 9). These ions are deflected by the strong radial electric field present around the upper corner, and strike the sidewall at rather small angles φ_1 (with respect to the local surface normal, see Fig. 9). It should be noted that, because of their small impact angles (closer to the surface normal), these ions lose a considerable fraction of their kinetic energy and contribute to the low-energy peak of the fast neutral energy distribution [Fig. 10(b)]. The other feature (at smaller angles) of the fast neutral angular distribution seems to originate from ions striking the lower part of the sidewall (right-hand side trajectory of Fig. 9). These ions did not fly near the corner and as a result are not deflected as much. The impact angle φ_2 is relatively large, and the resulting fast neutrals should retain a larger fraction of the parent ion kinetic energy. The energy distribution of these neutrals reflects the double-peaked distribution of the parent ions [see feature between ~20–56 eV in Fig. 10(b)]. The fast neutral flux must be much higher than the ion flux at the bottom of the cylindrical well (AB of Fig. 6). This can be understood from the fact that the ion flux at the bottom is only ~6% of the open area value (Fig. 6). Thus, the vast majority of ions entering through the mouth of the cylindrical well strike the sidewall, only to be reflected as fast neutrals on the bottom of the well. The fast neutral flux is also quite high near the outer sidewall of horizontal surface EF (compare to the step case of Ref. 1). The fast neutral angular distributions were single peaked near the outer foot of the ring (not shown) because surface EF is facing an open area. However, because most ions strike the outer sidewall at small angles (with respect to the normal on the sidewall), ions deposit most of their energy on the wall and the reflected neutrals do not have appreciable kinetic energy.

It should be noted that the results presented in this work depend critically on the thickness of the sheath compared to the size of the surface feature. For thicker sheaths (smaller ion density and larger sheath potential), ions are more directional (along the vertical), the ion flux along the bottom surfaces is higher, any deflected ions strike the sidewalls at more grazing angles, and the energy of the resulting neutrals is larger. In fact, a sheath much thicker than the feature size may be necessary to achieve anisotropic etching without significant sidewall erosion.

It should also be noted that, under the present conditions, the ion momentum exchange frequency ν_m is much smaller than the ion–plasma frequency. Thus, the drag term in the ion momentum equations [last term in Eqs. (5) and (6)] does not make a significant contribution to the ion transport.

IV. SUMMARY AND CONCLUSIONS

A combined fluid/MC simulation model was developed to study plasma molding over an axisymmetric surface feature; a Si ring on an otherwise flat Si surface. The fluid simulation predicted the two-dimensional (r,z) spatiotemporal profiles of the electric field, ion density, and ion flux over the feature. Using the electric-field profiles from the fluid simulation, trajectories of ions and energetic neutrals (formed by ion neutralization on the sidewalls or by charge-exchange collisions in the gas phase) were followed by a MC method to obtain the energy and angular distributions of energetic particles striking the substrate surface.

For a feature size comparable to the sheath thickness, the plasma–sheath interface was distorted according to the surface topography. Strong radial electric fields near the feature diverted oncoming ions away from the vertical. Deflected ions impinging on the sidewalls were assumed to reflect as energetic neutrals. Because of ion deflection, the ion flux decreased monotonically along the horizontal surface as one approached the outer sidewall from the open space. The ion flux was very low (~6% of the undisturbed value away from the ring) on the bottom of the cylindrical well formed by the ring. The ion density near the wall was lower by an order of magnitude compared to the "free stream" value. Ion depletion was more pronounced inside the cylindrical well where the surface-to-volume ratio was larger. The lower ion density resulted in a locally thicker sheath and smaller spread of the double-peaked IED at the bottom of the cylindrical well, compared to the IED on the horizontal surface outside the ring. The flux of fast neutrals (produced mainly by ion neutralization on the sidewalls) was larger than the ion flux at the bottom of the cylindrical well. The ion impact angle on

Downloaded 09 Sep 2003 to 129.7.158.16. Redistribution subject to AIP license or copyright, see http://ojps.aip.org/japo/japcr.jsp

the horizontal surfaces was progressively larger as the sidewall was approached from either side (inside or outside the cylindrical well). The fast neutral angular distribution at the bottom of the cylindrical well had two major features. The corresponding fast neutral energy distribution had a main feature at low energies and a broad feature at large energies, the latter reflecting the double-peaked energy distribution of the parent ions.

ACKNOWLEDGMENTS

Financial support by the National Institute of Standards and Technology, the National Science Foundation (Grant No. CTS-0072854), and Sandia National Laboratories is greatly appreciated.

[1] D. Kim and D. J. Economou, IEEE Trans. Plasma Sci. **30**, 2048 (2002).
[2] P. A. Miller and M. E. Riley, J. Appl. Phys. **82**, 3689 (1997).
[3] T. Panagopoulos and D. J. Economou, J. Appl. Phys. **85**, 3435 (1999).
[4] M. A. Sobolewski, J. K. Olthoff, and Y. Wang, J. Appl. Phys. **85**, 3966 (1999).
[5] E. A. Edelberg, A. Perry, N. Benjamin, and E. S. Aydil, J. Vac. Sci. Technol. A **17**, 506 (1999).
[6] J. R. Woodworth, M. E. Riley, P. A. Miller, G. A. Hebner, and T. W. Hamilton, J. Appl. Phys. **81**, 5950 (1997).
[7] I. W. Rangelow and H. Loschner, J. Vac. Sci. Technol. B **13**, 2394 (1995).
[8] *Handbook of Plasma Processing Technology*, edited by S. M. Rossnagel, J. J. Cuomo, and W. D. Westwood (Noyes, Park Ridge, NJ, 1990).
[9] S. Panda, D. J. Economou, and L. Chen, J. Vac. Sci. Technol. A **19**, 398 (2001).
[10] P. J. Wilbur, R. G. Jahn, and F. C. Curran, IEEE Trans. Plasma Sci. **19**, 1167 (1991).
[11] D. T. K. Kwok, Z. M. Zenh, P. Chu, and T. E. Sheridan, IEEE Trans. Plasma Sci. **27**, 225 (1999).
[12] J. R. Woodworth, P. A. Miller, R. J. Shul, I. C. Abraham, B. P. Aragon, T. W. Hamilton, C. G. Willison, D. Kim, and D. J. Economou, J. Vac. Sci. **21**, 147 (2003).
[13] D. Kim, D. J. Economou, J. R. Woodworth, P. A. Miller, R. J. Shul, B. P. Aragon, T. W. Hamilton, and C. G. Willison, IEEE Trans. Plasma Sci. (to be published).
[14] D. Kim and D. J. Economou, JSME Int. J., Ser. B **45**, 117 (2002).
[15] S. T. Zalesak, J. Comput. Phys. **31**, 335 (1979).
[16] A. F. Emery, J. Comput. Phys. **2**, 306 (1968).
[17] B. A. Helmer and D. B. Graves, J. Vac. Sci. Technol. A **16**, 3502 (1998).

Downloaded 09 Sep 2003 to 129.7.158.16. Redistribution subject to AIP license or copyright, see http://ojps.aip.org/japo/japcr.jsp